ADVANCED MATERIALS

DOI: 10.1002/adma.200602330

Magnetic and Electrical Characterizations of Half-Metallic Fe_3O_4 Nanowires**

By *Mu-Tung Chang*, *Li-Jen Chou*,* *Chin-Hua Hsieh*, *Yu-Lun Chueh*, *Zhong Lin Wang*, *Yasukazu Murakami*, and *Daisuke Shindo*

Half-metallic materials, such as CrO_2, $La_{0.7}Sr_{0.3}MnO_3$ (LSMO), and Fe_3O_4 are highly attractive for spintronics applications because of their high spin polarization.[1] Among these materials, magnetite (Fe_3O_4) is superior to others because of its high Curie temperature (T_c) of 858 K, which is crucial for thermal stability in device applications. In addition, magnetite has proven to be a ferromagnetic material with a high spin polarization (ca. 100 %) at the Fermi level, which results in a metallic minority spin channel and a semiconductor majority spin channel. Besides the utilization of spin electronics, magnetite can also be used as catalyst and in tunneling magnetoresistance (TMR) and giant magnetoresistive (GMR) devices.[2]

Previously, various studies in electron transport and magnetoresistance (MR) of magnetite have mainly focused on 2D structures, such as epitaxial thin films,[3] polycrystalline films,[4] and nanoclusters.[5] Recently, the electronic characteristics of 1D magnetite nanostructures have received much attention because of their unique electron-transport behaviors, which may be different from those of the bulk.[6] In addition, low-dimensional Fe_3O_4 nanoparticles are particularly promising in biomedical applications, such as drug transport/delivery, cell separation and imaging, and therapeutic in vivo technologies.[7] In this study, a simple vapor–solid growth method was applied to grow α-Fe_2O_3 NWs in an oxygen-deficient environment; magnetite NWs were then formed by converting the vertically aligned α-Fe_2O_3 NWs template in a reductive atmosphere. An extensive investigation on the mechanism of transforming α-Fe_2O_3 NWs to Fe_3O_4 NWs has been published elsewhere.[8] Electrical measurements were performed by fabricating nanodevices in which the NWs were laid on top of the designed Si chips. The Verwey temperature-transition phenomenon was observed in low-temperature measurements of the nanodevices. The magnetic behavior of the NWs was investigated by superconducting quantum interference device (SQUID) measurements. In addition, a magnetic flux map was acquired by electron holography, which revealed the magnetic microstructure of the 1D magnetite nanowires.[9]

Figure 1A and B shows a top-view morphology image of α-Fe_2O_3 and Fe_3O_4 NWs, respectively. After the reduction process, the morphology of the Fe_3O_4 NWs was very similar to that of the α-Fe_2O_3 template. Figure 1C shows a transmission electron microscopy (TEM) image of the magnetite NWs; the high-resolution TEM (HRTEM) image of the modulated α-Fe_2O_3 NW due to the oxygen deficiency and the magnetite diffraction pattern (DP) are shown in the insets of the image. The HRTEM image in Figure 1D reveals the single-crystalline structure of the NWs, without linear or planar defects. The two *d*-spacings of 0.29 nm were identified as Fe_3O_4 $\{02\bar{2}\}$ planes. The diffraction pattern, shown in the inset in Figure 1D, also illustrates the single-crystal nature of the NWs at the [111] zone axis.

Figure 2A shows a scanning electron microscopy (SEM) image of the nanodevices; an enlarged image of one of the devices in Figure 2A is shown in Figure 2B. The two-point *I*–*V* measurements were performed at room temperature in a LabView controlled measurement system under ambient conditions. The linear *I*–*V* curves (shown in Fig. 2C) indicate that the characteristics fit well to Ohm's law. The zero-field resistivities of the nanodevices were estimated by the following equation: $R = \rho L/A$ (R: resistance, ρ: resistivity, A: cross-section area, L: NW length). The diameter and length of the measured NWs were 25 nm and 0.7526 μm, respectively. Assuming that the Fe_3O_4 NWs were of a circular cross-section, the obtained resistivity was 10.30 Ω cm; approximately three orders of magnitude larger than that of bulk magnetite crystal (19 000 μΩ cm).[4a] The large measured difference between the NWs and the single crystal may be due to contact resistance and surface scattering, resulting from the high surface ratio. However, the surface-scattering mechanism, based on the Fuchs–Sonderheimer (FS) theory, indicates that the aspect ratio is an important factor to the total resistance of nanostructures.[10] According to FS theory, when surface scattering is the dominant mechanism the resistivity of a nanowire de-

[*] Prof. L.-J. Chou, M.-T. Chang, C.-H. Hsieh, Dr. Y.-L. Chueh
Department of Materials Science and Engineering
National Tsing Hua University
Hsinchu, Taiwan 300 (ROC)
E-mail: ljchou@mx.nthu.edu.tw
Dr. Y.-L. Chueh, Prof. Z. L. Wang
School of Materials Science and Engineering
Georgia Institute of Technology
Atlanta, GA 30332-0245 (USA)
Dr. Y. Murakami, Prof. D. Shindo
Institute of Multidisciplinary Research for Advanced Materials
Tohoku University
Sendai 980-8577 (Japan)

[**] This research was supported by the National Science Council through Grant No. NSC 94-2215-E-007-019, and partially supported by the exchanged program of Rotary Yoneyama foundation in Japan and Taiwan.

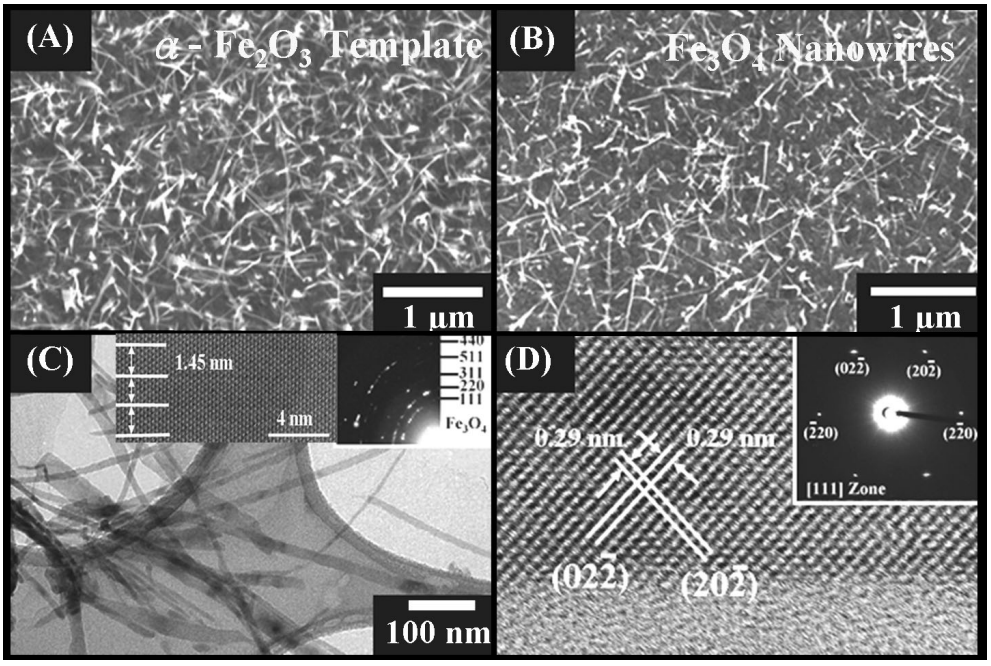

Figure 1. A) Scanning electron microscopy (SEM) image of α-Fe_2O_3 NWs synthesized on an FeNi alloy substrate. B) SEM image of the magnetite nanowires after the reduction process. C) Transmission electron microscopy (TEM) image of magnetite NWs; the high-resolution TEM image of the modulated α-Fe_2O_3 NWs, resulting from oxygen deficiency, and the magnetite diffraction pattern (DP) are shown in the upper corner inset. D) High-resolution TEM image of a magnetite NW.

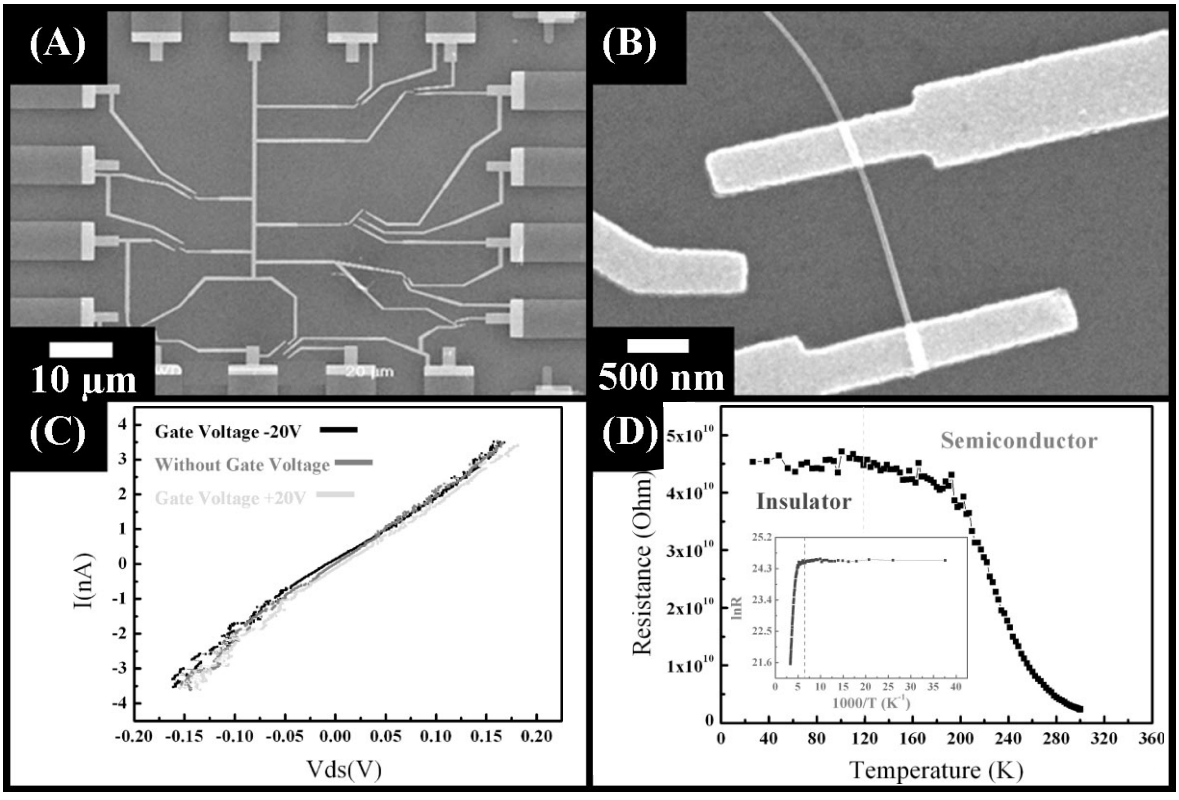

Figure 2. A) SEM image of the configuration of the nanodevices. B) Enlarged image of the device show in (A). C) *I–V* characteristics measured in various gate biases. and D) the resistances measured at different temperatures.

ADVANCED MATERIALS

creases with increasing wire width.[11] The positive slopes of the temperature versus resistance curves indicate that the larger the surface scattering, the higher the temperature.[11] In our case, however, the curves did not show this trend, as shown in Figure 2D. The extraordinary high resistivity may not be the result of the surface-scattering mechanism.

The Verwey transition, which was reported by Verwey and Haayman, is a special theory that describes the charge transportation mechanism for Fe_3O_4.[12] Theoretically, magnetite is a mixed-valency 3d transition metal compound, in which one third of the iron ions occupy tetrahedral A sites (all Fe^{3+}), and two thirds of the iron ions occupy octahedral B sites (one half of which as Fe^{2+} and the other half as Fe^{3+}, both in B2 and B3 sites[13]). The Verwey transition may be related to the ordering of the Fe irons, although the mechanism is still controversial. The dc conductivity increased abruptly by two orders of magnitude (from 10^{-1} to 10^{1} $\Omega^{-1}\,cm^{-1}$) as the measured temperature increased above the Verwey transition temperature (T_v).[14] Previous studies indicated that the electrical properties of Fe_3O_4 changed during the Verwey transition. This may be attributable to a transformation of its electronic state, which may strongly depend on the equilibrium positions of Fe atoms in the lattice. In our study, the magnetite NWs were obtained from hematite NWs, which exhibit oxygen vacancy modulation properties, while the size confinement of the 1D nanowires and the oxygen vacancy modulations resulted in the formation of charge ordering of iron ions at the B sites of the magnetite NWs. The charge ordering effect hindered carrier movement, which seemed to be the main reason for the discrepancy between our single-crystal NWs and bulk Fe_3O_4 crystal.

In Figure 2D, the data indicate that the resistance is a function of the temperature. As the temperature increases above 120 K, the NWs show semiconductor behavior. Below 120 K, the NWs show insulator characteristics. This suggests that carrier hopping is frozen at a temperature close to 120 K. In addition, the Arrhenius plot, ($\ln(R) \sim 1000/T$, shown in the inset of Fig. 2D) suggests that the transport mechanism is dominated by thermal activation at high temperatures (200–300 K). The thermal-activation model predicts that the conductivity follows the equation

$$\sigma(T) = \sigma_0 \exp(-\Delta E/k_B T) \quad (1)$$

where σ is the conductivity, k_B is the Boltzmann constant, and ΔE is the activation energy. From the slope of the $\ln(R) \sim 1000/T$ curve an activation energy of $\Delta E \approx 0.154$ eV was estimated. This value is in good agreement with reported values for magnetite core/shell nanowires[6a] and magnetite nanotubes.[6b]

For the magnetic measurements, the magnetite NWs were dispersed on a Si substrate to avoid mixed signals from the FeNi alloy substrate. Figure 3 shows the magnetization of magnetite NWs as a function of temperature in an applied field of 500 Oe ($1\ Oe = 1000/(4\pi)\ A\,m^{-1}$) between 2 and 300 K using field cooling (FC) and zero-field cooling (ZFC)

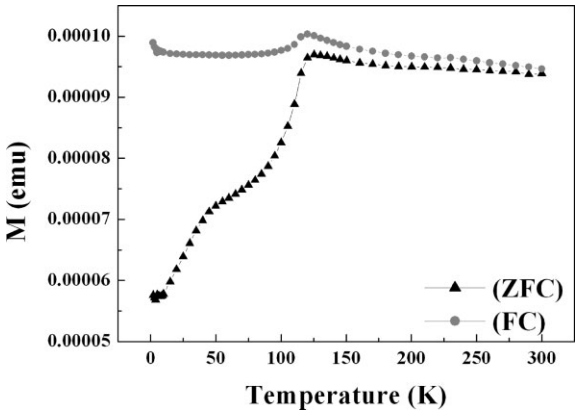

Figure 3. Magnetization of magnetite NWs as a function of temperature in the applied field of 500 Oe between 2 to 300 K using field cooling (FC) and zero-field cooling (ZFC) procedures.

procedures. When the specimen was treated by ZFC, the individual magnetic moments were randomly oriented at 2 K. Upon applying the external magnetic field, the original random distributed moments were forced to align along the applied field. The magnetization M increased with the temperature, and reached a maximum value at 125 K, which is defined as the blocking temperature (T_B). At this temperature, the energy of the aligned magnetic moments is balanced with the thermal energy. Above this temperature thermal perturbation destroys the alignment of the moments. Both ZFC and FC magnetization curves exhibited a maximum moment at a T_B value of ca. 125 K. Below T_B, the ZFC curve shows a gradual increase as the moments progressively reorient along the applied field at low temperatures (2–125 K), while the FC curve shows a flat line at a low temperature because of saturation of the magnetic moment. Similar results have been observed in magnetite nanoparticles[15] and ultrathin magnetite films.[16]

In addition, both ZFC and FC magnetization show an abrupt increase at the Verwey transition temperature of about 120 K. The structure transition results in a change of the electrical and magnetic properties at 120 K.[17] The large divergence of ZFC and FC (below 300 K) resulted from the large amounts of magnetic isotropy energy contributed by the external magnetic field during the cooling process. Hence, it may be also the reason why the ZFC and FC curves decrease slightly above 125 K.[18]

The magnetization distribution in the Fe_3O_4 nanowires was examined by electron holography, which deduces the magnetic information from the phase shift of electrons. Figure 4A shows a bright-field image of the nanowires supported on an amorphous microgrid carbon film. The nanowire marked as "X" makes contact with another nanowire, "Y". Figure 4B shows a reconstructed phase image, acquired in the rectangular area of Figure 4A. A transparent bright-field image was superimposed on the contour map in Figure 4B to clarify the position of nanowires—refer to the gray contrast. Strictly speaking, the phase shift of electrons was due not only to the

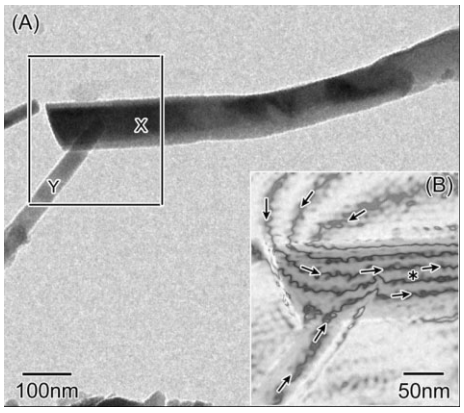

Figure 4. Electron hologram, indicating the magnetization distribution in the magnetite nanowires.

magnetic field but also to the electric field (i.e., mean inner potential of the specimen).[9a–c] We removed the unwanted signal originating from the mean inner potential by the "time-reversal operation of an electron beam" method, proposed by Tonomura et al.[19] Therefore, Figure 4B displays only the magnetic information. The contour lines and arrows in Figure 4B represent the lines of magnetic flux and their directions, respectively. An essential point is that the magnetic flux is parallel to the longitudinal axis of the nanowires. Several specimens having small diameters (on the order of 10 nm) were observed by the holography technique, but we were unable to find any magnetic domain walls. The figure also demonstrates that some amount of magnetic flux leaks out of the nanowires, as can be seen from the leakage near the terminal end (Fig. 4B), wherein the flux lines are no longer parallel to the nanowire. Apparently, the shape anisotropy dominates the magnetization distribution in these nanowires, and the result is consistent with the small magnetocrystalline anisotropy in cubic Fe_3O_4 at room temperature. We have estimated the magnetic flux density B of the nanowire X by following the equation $B = h/(etl)$, where h stands for Planck's constant, e is the elementary electric charge, t the specimen thickness, and L the spacing of the contour lines in the reconstructed phase image. The magnetic flux density B was evaluated at 0.46 T at the position of the asterisk in Figure 4B. The parameter t was estimated at 122 nm assuming a mean inner potential of 12.0 V, which was deduced from the phase shift in the rod-shaped nanowire Y; further details on thickness measurements by holography have been described elsewhere.[9a] The measured flux density was somewhat lower than that of bulk Fe_3O_4 (0.60 T). A possible source for the discrepancy may be surface spin disorder, which is significant in nanowires with a large surface-to-volume ratio. Furthermore, the flux density appears to be sensitive to the crystallinity of nanowires. The observations in Figure 4 imply the possibility of regulating the spin current with the half-metallic nanowires due to the controlled magnetization distribution in the 1D form. On the other hand, special attention should be paid to surface disorder, which degrades the spin polarity.

In summary, high quality and uniform Fe_3O_4 nanowires were produced by converting α-Fe_2O_3 template nanowires in a reductive atmosphere. The microstructures of the nanowires show single-crystal features. Electron transport properties were investigated, and the Verwey temperature transition phenomenon was observed by low-temperature measurements of the nanodevices. Size confinement and oxygen vacancy modulations resulted in the formation of charge ordering of iron ions, which may be attributable for the high resistance of the single-crystal NWs compared with that of bulk Fe_3O_4 crystal. The carrier-hopping mechanism was found to be frozen at a temperature close to 120 K. SQUID measurements indicated that the blocking temperature phenomenon was due to the electronic status of the NWs. The magnetic flux density of the NWs was measured and described for the first time by using electron holography. No domain walls were observed for NWs with diameters under 10 nm; the magnetic flux was parallel to the longitudinal axis of the nanowires. The magnetic flux density B was evaluated and compared to bulk Fe_3O_4. These results imply the possibility of regulating spin current with the half-metallic nanowires because of the controlled magnetization distribution in the 1D form.

Experimental

A typical Zimberger-made three-zone tube furnace system, including a vacuum pump, a gas flow system, and a quartz/alumina tube combination, was used to synthesize the NWs. The vacuum level of this configuration was higher than 3×10^{-2} Torr (1 Torr $\approx$ 133.3 Pa); the annealing temperature could reach a maximum of ca. 1500 °C. After the α-Fe_2O_3 NWs were synthesized on a FeNi substrate magnetite NWs were fabricated by converting the α-Fe_2O_3 template NWs in a mixed reductive atmosphere of H_2 (5 %) + Ar (95 %), while the temperate was maintained at 450 °C for 20 min. The surface morphology was examined by using a field-emission scanning electron microscope (JSM-6500F) operated at 15 kV. A field-emission transmission electron microscope (JEM-3000F), operated at 300 kV with a point-to-point resolution of 0.17 nm, was used to obtain information on the microstructures. Electrical measurements were performed by sequential procedures, including the definition of electrodes by electron-beam lithography, metal evaporation, and device evaluation. The sample with the NWs grown on the surface was brought into tight contact with the designed pattern substrate with a common clip, followed by transfer of the NWs from the sample surface to the designed pattern substrate by ultrasonic vibration. The field-emission scanning electron microscope (FESEM, JOEL JSM-6500F) was used to locate the positions of the randomly dispersed nanowires on the chips. Ni (35 nm) and Au (65 nm) were selected as contact electrode materials. The width of the electrodes on the nanowires was designed to be 0.2 μm. A cold field-emission scanning electron microscope (SEM FEI-SIRION) with a nanopattern generation system (NPGS) was used for this purpose. A LabView program was used to control the *I–V* testing process. Electron holography was performed by using another JEM-3000F dedicated to magnetic domain observations, that is, the microscope had a magnetic-shielded objective lens, in which the magnetic field was reduced to 0.6 mT. A superconducting quantum interference device (SQUID, Quantum Design, MPMS5 with a biprism setup) was used to measure the magnetic properties of the NWs.

Received: October 13, 2006
Published online: July 26, 2007

ADVANCED MATERIALS

[1] a) H. Y. Hwang, S. W. Cheong, *Science* **1997**, *278*, 1607. b) J. H. Park, E. Vescovo, H. J. Kim, C. Kwon, R. Ramesh, T. Venkatesan, *Nature* **1998**, *392*, 794. c) Z. Zhang, S. Satpathy, *Phys. Rev. B* **1991**, *44*, 13 319.

[2] a) M. N. Baibich, J. M. Broto, A. Fert, F. Nguyen Van Dau, F. Petroff, P. Etiene, G. Creuzet, A. Friederich, J. Chazelas, *Phys. Rev. Lett.* **1988**, *61*, 2472. b) W. Eerenstein, T. T. M. Palstra, S. S. Saxena, T. Hibma, *Phys. Rev. B* **2002**, *66*, 201 101.

[3] a) G. Q. Gong, A. Gupta, G. Xiao, W. Qian, V. P. Dravid, *Phys. Rev. B* **1997**, *56*, 5096. b) X. W. Li, A. Gupta, G. Xiao, G. Q. Gog, *J. Appl. Phys.* **1998**, *83*, 7049.

[4] a) J. M. D. Coey, A. E. Berkowitz, L. I. Balcells, F. F. Putris, F. T. Parker, *Appl. Phys. Lett.* **1998**, *72*, 734. b) D. L. Peng, T. Asai, N. Nozawa, T. Hihara, K. Sumiyama, *Appl. Phys. Lett.* **2002**, *81*, 4598.

[5] M. Venkatesan, S. Nawka, S. C. Pillai, J. M. D. Coey, *J. Appl. Phys.* **2003**, *93*, 8023.

[6] a) D. Zhang, Z. Liu, S. Han, C. Li, B. Lei, M. P. Stewart, J. M. Tour, C. Zhou, *Nano Lett.* **2004**, *4*, 2151. b) Z. Liu, D. Zhang, S. Han, C. Li, B. Lei, W. Lu, J. Fang, C. Zhou, *J. Am. Chem. Soc.* **2005**, *127*, 6.

[7] G. Reiss, A. Hutten, *Nat. Mater.* **2005**, *4*, 725.

[8] Y. L. Chueh, M. W. Lai, J. Q. Liang, L. J. Chou, Z. L. Wang, *Adv. Funct. Mater.* **2006**, *16*, 2243.

[9] a) D. Shindo, T. Oikawa, *Analytical Electron Microscopy for Materials Science*, Springer, Tokyo **2002**. b) A. Tonomura, *Electron Holography*, 2nd ed., Springer, Tokyo **1999**, p. 78. c) E. Volkl, L. F. Allard, D. C. Joy, *Introduction to Electron Holography*, Kluwer Academic/Plenum, New York **1999**.

[10] a) K. Fuchs, *Proc. Cambridge Philos. Soc.* **1938**, *34*, 100. b) E. H. Sondheimer, *Adv. Phys.* **1952**, *1*, 1. c) K. L. Chopra, *Thin Film Phenomena*, McGraw-Hill, New York **1969**, p. 345.

[11] W. Wu, S. H. Brongersma, M. van Hove, K. Maex, *Appl. Phys. Lett.* **2004**, *84*, 2838.

[12] E. J. W. Verwey, P. W. Haayman, *Physica* **1941**, *8*, 979.

[13] J. H. Park, L. H. Tjeng, J. W. Allen, P. Metcalf, C. T. Chen, *Phys. Rev. B* **1997**, *55*, 12 813.

[14] F. Walz, *J. Phys. Condens. Matter* **2002**, *14*, R285.

[15] T. Yang, C. Shen, Z. Li, H. Zhang, C. Xiao, S. Chen, Z. Xu, D. Shi, J. Li, H. Gao, *J. Phys. Chem. B* **2005**, *109*, 23 233.

[16] F. C. Voogt, T. T. M. Palstra, L. Niesen, O. C. Rogojanu, M. A. James, T. Hibma, *Phys. Rev. B* **1998**, *57*, 8107.

[17] W. Kim, K. Kawaguchi, N. Koshizaki, M. Sohma, T. Matsumoto, *J. Appl. Phys.* **2003**, *93*, 8032.

[18] A. J. Rondinone, A. C. S. Samia, Z. J. Zhang, *J. Phys. Chem. B* **1999**, *103*, 6876.

[19] A. Tonomura, T. Matsuda, T. Endo, J. Arii, K. Mihama, *Phys. Rev. B* **1986**, *34*, 3397.

